

Investigation of O interstitial diffusion in β -Ga₂O₃: direct approach via master diffusion equations

Grace McKnight and Channyung Lee

*Department of Mechanical Science and Engineering, University of Illinois at Urbana-Champaign,
1206 W. Green Street, Urbana, Illinois 61801, United States.*

Elif Ertekin

*Department of Mechanical Science and Engineering, University of Illinois at Urbana-Champaign,
1206 W. Green Street, Urbana, Illinois 61801, United States. and
Materials Research Laboratory, University of Illinois at Urbana-Champaign, Urbana, Illinois 61801**
(Dated: March 4, 2025)

Monoclinic β -Ga₂O₃, a promising wide band gap semiconducting material, exhibits complex, anisotropic diffusional characteristics and mass transport behavior as a result of its low symmetry crystal structure. From first-principles calculations combined with master diffusion equations, we determine three-dimensional diffusion tensors for neutral (O_i⁰) and 2- charged oxygen interstitials (O_i²⁻). Systematic exploration of the configurational space identifies stable configurations in these two dominant charge states and their corresponding formation energies. By connecting every pair of low-energy configurations considering both interstitial or interstitialcy hops, we construct three-dimensional diffusion networks and evaluate hopping barriers of all transition pathways in networks. Combining the collection of (i) defect configurations and their formation energies and (ii) the hopping barriers that link them, we construct and solve the master diffusion equations for O_i⁰ and O_i²⁻ separately through the Onsager approach, resulting in respective three-dimensional diffusion tensors D_{O_i⁰} and D_{O_i²⁻}. Both O_i⁰ and O_i²⁻ present the fastest diffusion along the *b*-axis, demonstrating significant anisotropy. The predicted self-diffusivities along [100] and $\bar{2}01$ align well with previously reported values from isotopically labeled oxygen tracer experiments, highlighting the reliability of the approach in capturing complex diffusion mechanisms.

I. INTRODUCTION

Beta gallium oxide (β -Ga₂O₃) has garnered interest as a wide band gap semiconductor due to its large band gap of 4.8 eV [1–3], high breakdown electric field [4], and notable thermal stability [5, 6]. These unique properties make it ideal for high-power and high-frequency electronic devices, such as power transformers, UV photo-detectors, solar cells, and sensors subject to extreme conditions [7–11]. Advances in the synthesis of high-quality β -Ga₂O₃ single crystal wafers [6, 12, 13] and thin-films [14–16] have further enhanced its potential. Compared to its predecessors, silicon carbide (SiC) and gallium nitride (GaN), β -Ga₂O₃ offers distinct advantages, positioning it as a crucial material for future power electronics and optoelectronic applications.

In semiconducting materials of interest for power electronics like β -Ga₂O₃, realizing their full potential requires a detailed understanding of intrinsic defect diffusion, as it plays a crucial role in determining electrical performance and device stability. In particular, the low-symmetry monoclinic crystal structure of β -Ga₂O₃ presents multiple diffusion pathways and directionally distinct defect interactions, making defect transport mechanisms especially rich and challenging to understand. Failing to control defect migration can cause unintended mass transfer, phase segregation, defect clustering, and reduced reliability [17–19]. A thorough investigation of native diffusion behavior lays the groundwork for precisely tailoring material properties to suit device-specific applications. This is

especially important in anisotropic semiconductors, where native defects significantly influence direction-dependent properties.

Oxygen ion diffusion in semiconducting oxides typically occurs via either vacancy- or interstitial-mediated mechanisms. Although most oxides demonstrate vacancy-dominated O transport, materials characterized by O_i transport exhibit exceptionally low diffusion activation energies (E_{act}) [20]. Computational studies of β -Ga₂O₃ predicted barriers as low as 0.14 eV for O_i [21]. Experimental observation of O self-diffusion coefficients vary from 3.35×10^{-16} cm²/s at 300 K [22] to 5.8×10^{-13} cm²/s at 1500 K [23–25]. Moreover, in many wide band gap metal oxides including β -Ga₂O₃ [26, 27], the Fermi energy (E_{Fermi}) frequently appears close to the conduction band minimum (CBM). This high E_{Fermi}, associated with intentional or unintentional donor impurities, reduces the formation energies of negatively charged O_i, promoting the role of O_i in O diffusion [28].

O_i diffusion is also practically important for tuning properties of semiconducting oxides. For example, in ZnO and TiO₂, the injection and subsequent diffusion of O_i can help suppress unintentional V_O acting as unwanted donors that degrade carrier mobilities [29–31]. Although conventional doping methods are often limited by high-energy processing (e.g., ion implantation) or inadequate control (in-diffusion), recent studies have revealed that surface treatment can dramatically lower the kinetic barriers for O_i incorporation and formation. Injecting O from a clean, poison-free surface introduces O_i that propagates into the near-surface bulk, effectively annihilating V_O at previously unattainable low temperatures [22, 32], credited to notably low diffusion activation energies.

In this study, we employ a direct approach combining first-

* ertekin@illinois.edu

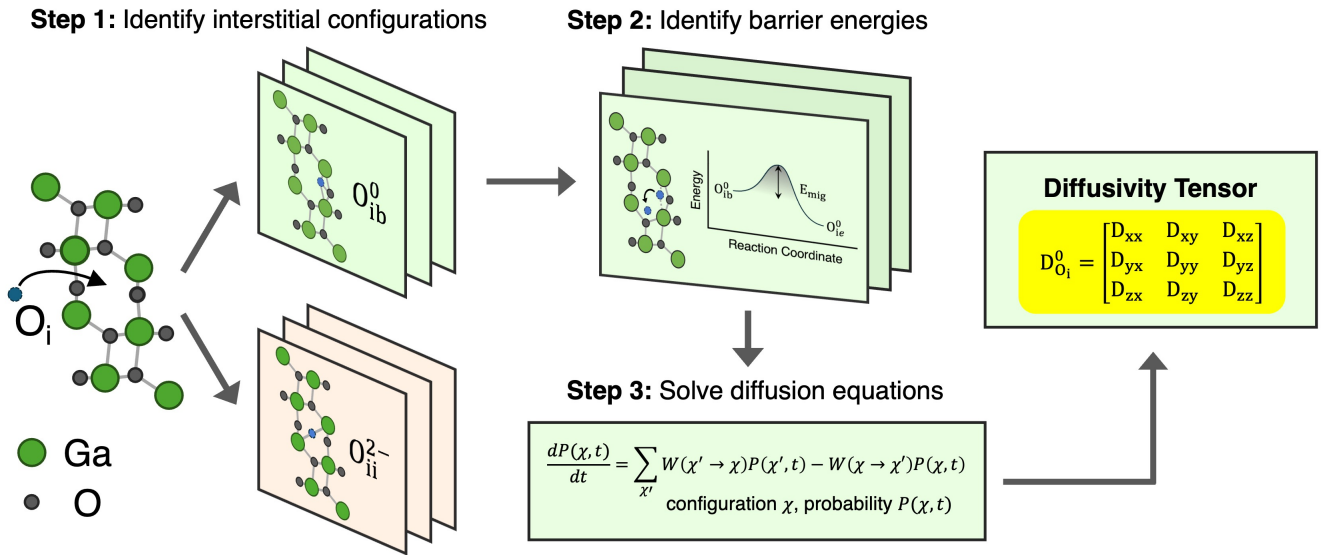


FIG. 1. Schematic workflow used to construct the three-dimensional diffusivity tensor adapted from Lee *et al.* [33].

principles calculations and the solution of the master diffusion equations to elucidate the full diffusion tensor for neutral and 2- charged O_i in β - Ga_2O_3 . We begin by systematically examining a wide range of O_i configurations, including split-interstitials, and determine their formation energies. We identify six O_i^0 and five O_i^{2-} low-energy configurations. Based on these configurations, we construct three-dimensional diffusion networks for each charge state, identifying 17 unique hops for O_i^0 and 28 for O_i^{2-} . Using defect formation energies (E_{form}) and migration barriers (E_{mig}), we assemble and solve the master diffusion equations, yielding three-dimensional diffusion tensors. Our results indicate that both O_i^0 and O_i^{2-} diffuse significantly faster along the b -axis, with diffusivities orders of magnitude higher than along the a^* - or c -axes. Comparisons to available ^{18}O tracer self-diffusion experiments demonstrate good agreement with our predictions. Finally, because of their lower diffusion barriers and formation energies, we conclude that O_i , opposed to V_O , is the likely dominant mediator of O transport in β - Ga_2O_3 . Our findings deepen understandings of intrinsic O diffusion in β - Ga_2O_3 , offering insights to guide future optimization of electronic devices.

II. METHODS

To predict the O_i three-dimensional diffusivity tensor, we employed the Onsager approach to construct and solve the master diffusion equations using the package Onsager [34–36]. The master diffusion equations are a set of coupled rate equations that describe transitions between different O_i configurations. Their solution results in the Onsager coefficients, i.e. the components of the diffusion tensor. Several simplifying assumptions are embedded in the master diffusion equa-

tion approach. We treat diffusion as a process in which defect configurations, undergoing harmonic motions, are described by a Markov process with well-defined beginning and end states that thermalize in between jumps. The defect concentrations are assumed to follow the grand canonical ensemble, where all species are exchangeable with reservoirs of fixed chemical potential, and site probabilities are governed by the Boltzmann distribution. Transition rates are determined by transition state theory, based on the obtained hopping barriers and site energies from one configuration to another.

These rates satisfy detailed balance in equilibrium. We define $P(\chi, t)$ as the probability of finding the system in state χ at time t , and express the rate of change of the probability as

$$\frac{dP(\chi, t)}{dt} = \sum_{\chi'} (W(\chi' \rightarrow \chi)P(\chi', t) - W(\chi \rightarrow \chi')P(\chi, t)). \quad (1)$$

Here, for a given configuration χ , the sum is taken over all other possible configurations χ' . The first term inside the summation, $W(\chi' \rightarrow \chi)P(\chi', t)$, represents the rate at which the system transitions from other states χ' into state χ , weighted by the probability of state χ' . The second term, $W(\chi \rightarrow \chi')P(\chi, t)$, similarly accounts for the rate at which the system leaves state χ to transition into other states χ' . By incorporating the site energies and migration barriers, we formulate a set of coupled rate equations. The solution of system of equations under equilibrium ($dP(\chi, t)/dt = 0$, and detailed balance) yields the three-dimensional diffusion tensor for each interstitial network. The diagonal elements of the tensor give the diffusion coefficients along the a^* , b , and c crystallographic directions, while the off-diagonal terms are the cross-diffusion coefficients. For additional mathematical and conceptual detail, refer to the original works describing the Onsager software package [34–37]. The overall workflow is illustrated in Figure 1.

In the first phase of our approach (Figure 1, Step 1), we compile a set of candidate O_i configurations using Voronoi tessellations [38], which partition the lattice into distinct regions around each lattice atom with boundaries defined by points equidistant from neighboring

lattice sites. These points serve as natural candidates for interstitial configurations that minimize repulsion between lattice and interstitial sites. This approach produced fifteen candidate structures, which we further complemented by configurations proposed in Ingebrigtsen *et al.* and Jeong *et al.* [22, 39] We relax these initial structures in two dominant charge states (neutral and 2- charged) [40, 41] using first-principles density functional theory (DFT) [42, 43] simulations to obtain site energies. We used the projector augmented wave (PAW) method [44, 45], as implemented in the Vienna Ab Initio Simulation Package (VASP) [46, 47], and the Perdew-Burke-Ernzerhof (PBE) approximation of the exchange-correlation functional [48]. Calculations employed a plane-wave basis set with a cutoff energy of 420 eV. The ground state lattice parameters of the monoclinic β -Ga₂O₃ conventional unit cell were determined to be $a = 12.28$ Å, $b = 3.05$ Å, $c = 5.82$ Å, and $\beta = 103.76^\circ$ for 1×4×2 supercell, and are consistent with other computational [49–51] and experimental studies [52, 53]. Defect structures were modeled in 160-atom supercells using the Monkhorst-Pack scheme [54] with a 2×2×2 k-point mesh. Geometry optimization of defect structures was performed with a convergence criterion of 1×10^{-4} eV for the total energy and 2×10^{-2} eV/Å for atomic forces.

The defect formation energy $E[\text{O}_i^q]$ (site energies) of an interstitial in charge state q is obtained using the supercell approach [55–57]:

$$E_{\text{for}}[\text{O}_i^q] = E_{\text{tot}}[\text{O}_i^q] - E_{\text{tot}}[\text{Bulk}] - \mu_{\text{O}} + qE_{\text{Fermi}} + E_{\text{corr}}, \quad (2)$$

where $E_{\text{tot}}[\text{O}_i^q]$ is the total energy of the defective supercell and $E_{\text{tot}}[\text{Bulk}]$ is the total energy of the pristine bulk supercell. The term μ_{O} is the chemical potential of oxygen in the system. The charge state is given by q , which can take the value of 0 or 2-, and E_{Fermi} accounts for the exchange of electrons from reference electron reservoir. Finally, the energy correction term, E_{corr} , accounts for the finite-size effects resulting from electrostatic interactions between charged defects in adjacent supercells. We utilized the method proposed by Lany and Zunger [56] to calculate the finite size effect corrections for potential alignment $\Delta E_{\text{pa}}(D, q)$ and image charge ΔE_i . For each charge state, we assemble an independent defect library containing relaxed configurations and their associated E_{for} . To down-select the number of defects included, only configurations with $E_{\text{for}} \leq 1.2$ eV relative to the lowest energy defect are used to construct the network, resulting in six O_i^0 and five O_i^{2-} configurations.

In the second phase (Figure 1, Step 2), we construct the hopping network by considering all possible transitions between interstitial pairs in the supercell, regardless of proximity. We saturated the unit cell of β -Ga₂O₃ with defects in our library and identify all possible symmetry-unique hops between pairs within 4 Å to populate the network. Since many of these hops can be decomposed into sequences of shorter, substituent hops, we use a down-selection approach to isolate independent hops, as discussed in Section III(B). We calculated migration barriers for each possible path using the climbing-image nudged elastic band method (ci-NEB) [58]. At this stage, the three-dimensional diffusion network is complete, providing all necessary inputs for the Onsager methodology.

In the third, final phase of the workflow (Figure 1, Step 3), we assemble and solve the master diffusion equations. These equations are constructed using the interstitial sites and their site energies, along with the transitions between them and associated energy barriers, comprising the hopping network. The master diffusion equations are derived from the Onsager reciprocal relations, which describe a generalized linear relationship between thermodynamic forces and fluxes. The constants of proportionality in this relationship represent diffusion coefficients. Details of the formulations, assumptions of the Onsager approach, and parameters used in the DFT simulations to compute site and transition energies are provided in the SI.

III. RESULTS AND DISCUSSION

A. Oxygen Interstitial Defect Configurations and Formation Energies

In highly anisotropic, monoclinic β -Ga₂O₃, local Ga-O bonding environments vary extensively, resulting in a broad spectrum of extended defects, including split configurations. Previous studies of Ga interstitials (Ga_i) and vacancies (V_{Ga}), for instance, have revealed that two distinct Ga sites (octahedral and tetrahedral) can adopt extended “N-split” configurations spanning multiple sites (e.g., $\text{Ga}_i\text{-V}_{\text{Ga}}\text{-Ga}_i$ or $\text{V}_{\text{Ga}}\text{-Ga}_i\text{-V}_{\text{Ga}}$ chains), which can be more stable than conventional point defects [33, 59]. Similarly, three inequivalent O sites, including two 3-fold configurations (trigonal planar coordination) and one 4-fold arrangement (distorted tetrahedron) can adopt multiple configurations, highlighting the need for a comprehensive examination of possible split O_i . In this work, we have identified total 11 symmetry-unique defect configurations, including both conventional and split O_i .

Figure 2(a-f) features six low-energy configurations of O_i^0 , while Figure 2(g-k) features five O_i^{2-} configurations, both of which are used to construct their respective defect libraries. These libraries include both split-interstitials (a-f,k), where the defective O shares a site with a lattice O atom, and traditional isolated interstitials (g-j) where the defective O sits in a channel with minimal displacement of lattice O atoms.

Among neutral interstitials, O_{ia}^0 exhibits the lowest formation energy of 2.68 eV (Figure 3), followed by O_{if}^0 , O_{ic}^0 , and O_{id}^0 , which have energies 0.05, 0.14, and 0.23 eV higher than O_{ia}^0 , respectively. These four neutral defects are all within the A channel (see Figure 2(l)), consistent with the trend observed in Blanco *et al.* [60]. The remaining two defects, O_{ib}^0 and O_{ic}^0 , within the B and C channels, are 0.76 and 0.62 eV higher than O_{ia}^0 , respectively. Other studies have also identified the split-interstitial O_{if} [27, 39, 61–64], as well as O_{ic} [65] and O_{ie} [62].

For charged interstitials, the defect in the A channel, $\text{O}_{\text{ig}}^{2-}$, exhibits the lowest E_{form} of 1.56 eV when E_{Fermi} is at 0.8 eV below the CBM. Two configurations close to the lattice in the B and C channels, $\text{O}_{\text{ih}}^{2-}$ and $\text{O}_{\text{ik}}^{2-}$, have E_{form} higher than that of $\text{O}_{\text{ig}}^{2-}$ by 0.52 and 0.69 eV, respectively. In contrast, $\text{O}_{\text{ii}}^{2-}$ and $\text{O}_{\text{ij}}^{2-}$, both in the centers of the B and C channels, exhibit the highest E_{form} , higher than that of $\text{O}_{\text{ig}}^{2-}$ by 1.06 and 1.23 eV, respectively.

Electrostatic interactions between lattice atoms and O_i likely drive this trend in $E_{\text{form}}[\text{O}_i^{2-}]$. For instance, $\text{O}_{\text{ig}}^{2-}$ sits farther from lattice O atoms within the A channel to reduce repulsive interactions, while simultaneously maintaining optimal distance to nearby Ga atoms to maximize electrostatic attractions. All other defects are relatively closer to lattice O atoms, farther away from Ga atoms, or both, consistent with the highest energy defects in the library. Other studies [21, 22, 39, 51, 60, 61, 65, 66] have reported two additional configurations in the center of the A channel. Geometry optimization reveals that the 2-fold coordinated configurations reported in Zimmermann *et al.* and Li *et al.* relax to O_{ig}' (Figure S1(b)). While the 3-fold coordinated configurations O_{ig}' and O_{ig}'' (Figure S1(c)) reported in Zimmermann *et al.*, Lehtom *et al.*, and Jeong *et al.* were confirmed stable, they were excluded from the diffusion network following a detailed analysis of diffusion pathways, as described in Section III(B). Overall, our predicted formation energies of neutral and charged O_i are in good agreement with those reported in Zacherele *et al.* and Peelars *et al.* [27, 51].

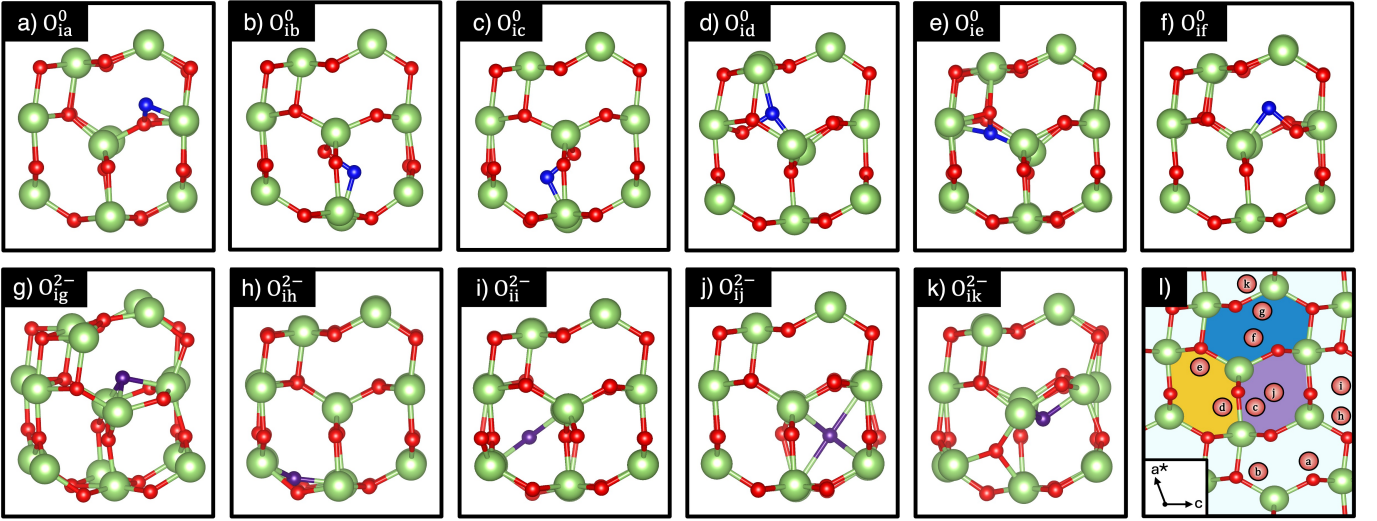


FIG. 2. Low-energy configurations of (a-f) O_i^0 and (g-k) O_i^{2-} . Schematic representation (l) of b -axis channels in β - Ga_2O_3 , conventionally named "A", "B", and "C", depicted in blue, gold, and purple, respectively, with labeled positions of unique O_i sites.

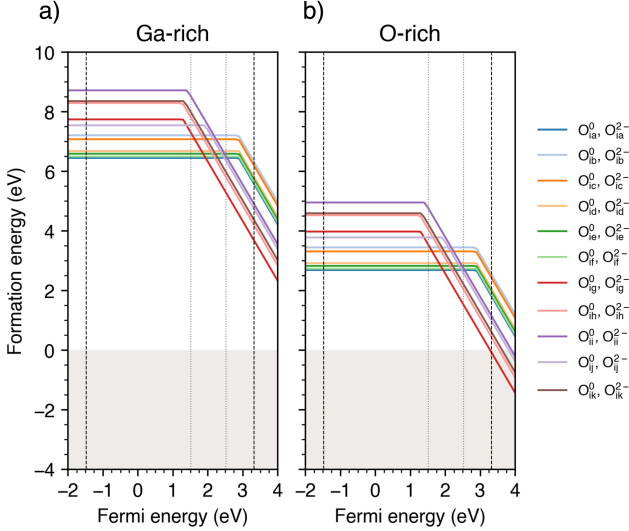


FIG. 3. Formation energies of various configurations of O_i as a function of Fermi-energy level using the PBE level of theory under (a) Ga-rich and (b) O-rich thermodynamic conditions. The dashed lines near the left and right sides of the plot are the HSE valence band maximum (VBM) and conduction band minimum (CBM) levels, respectively, predicted by band alignments using the electrostatic potentials between PBE and HSE band structures. The leftmost dotted line is the Fermi energy chosen to represent the neutral defects in the self-diffusivity plots (1.8 eV below CBM) and the rightmost dotted line is the Fermi energy chosen to represent the charged defects in the self-diffusivity plots (0.8 eV below CBM).

B. Diffusion Networks and Migration Activation Energies

To create diffusivity tensors, we identify and construct core sets of "principal hops" (PHs), the fundamental and indivisible migrations, for both the neutral and charged diffusion networks. In other words, a

PH is one that cannot be decomposed into a sequence of smaller transitions. To identify PHs, we enumerate all transitions between defect pairs across all possible sites of the supercell. For split-interstitial defects, we use a representative midpoint between two oxygen atoms to denote the defect site and efficiently track interstitialcy (kick-out) hops. In these hops, the original interstitial atom occupies the lattice site and the original lattice atom migrates as an interstitial.

Enumerating each possible migration from a defect-saturated supercell yields hundreds of pathways. To narrow these to a practical number, we remove symmetry-equivalent hops and systematically eliminate candidates that could be broken down into smaller PHs. For example, instead of a direct hop from O_{ia}^0 to O_{ic}^0 , inspecting intermediate configurations between them suggests that O_i migrates first through O_{ib}^0 , resulting in two PHs. We perform initial coarse NEB calculations to identify additional metastable states along selected paths and eliminate unrealistic paths with barriers exceeding 10 eV. When metastable intermediate configurations emerge, we conduct geometry relaxations to determine if they are within our network or new candidate defects. In all cases, these configurations match or closely resemble existing interstitials in our libraries. If migration barriers exceed 10 eV, we eliminate the hop. Through these down-selection processes, we reduce the number of hops in the neutral network from 125 to 17, and from 140 to 28 in the charged network. Once a single pathway cannot be decomposed into shorter hops, we perform a final NEB calculation with more stringent convergence criteria to identify the migration barrier, E_{mig} . These identified symmetry-unique PHs and corresponding E_{mig} 's for O_i^0 and O_i^{2-} are summarized in Tables S1 and S2, respectively. We then used the Onsager software package to find diffusivities of O_i^0 and O_i^{2-} ($D_{O_i^0}$ and $D_{O_i^{2-}}$) [36].

Figure 4(a,e) summarizes predicted diffusivities ($D(T)$) along the a^* , b , and c crystallographic directions, following the Arrhenius relationship below:

$$D(T) = D_0 \exp\left(-\frac{E_{\text{act}}}{k_B T}\right), \quad (3)$$

where D_0 is the pre-exponential factor and k_B is the Boltzmann constant. The shaded region indicates the incorporation of a ± 0.1 eV uncertainty on the calculated NEB barriers, to account for typical

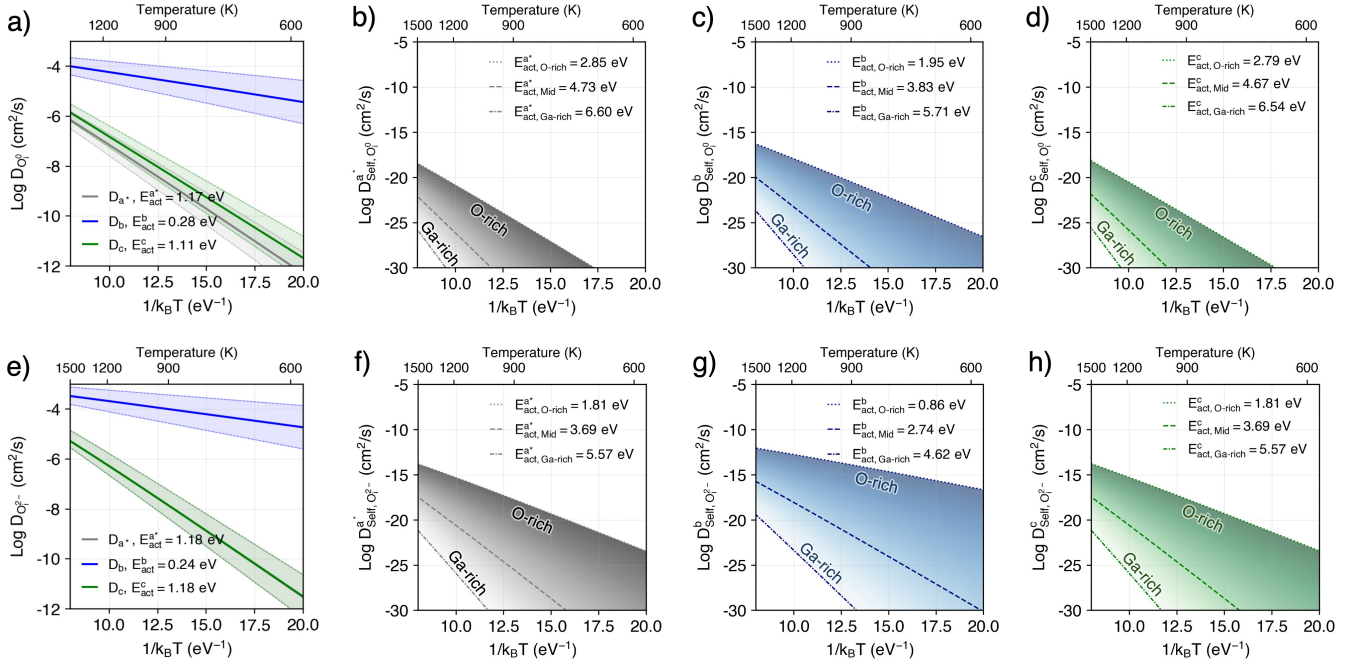


FIG. 4. Arrhenius plot of diffusivities of (a) O_i^0 and (e) O_i^{2-} . Shaded regions in (a) and (b) represent 0.1 eV uncertainty in E_{mig} . The remaining plots highlight self-diffusivities of (b, c, d) O_i^0 and (f, g, h) O_i^{2-} . Thermodynamic limits (Ga-rich and O-rich) are given within the dotted lines, where the dashed middle line indicates the midpoint between two limits. Activation energies (E_{act}) for various directions (a,e) and thermodynamic conditions (a-c,f-h) are indicated.

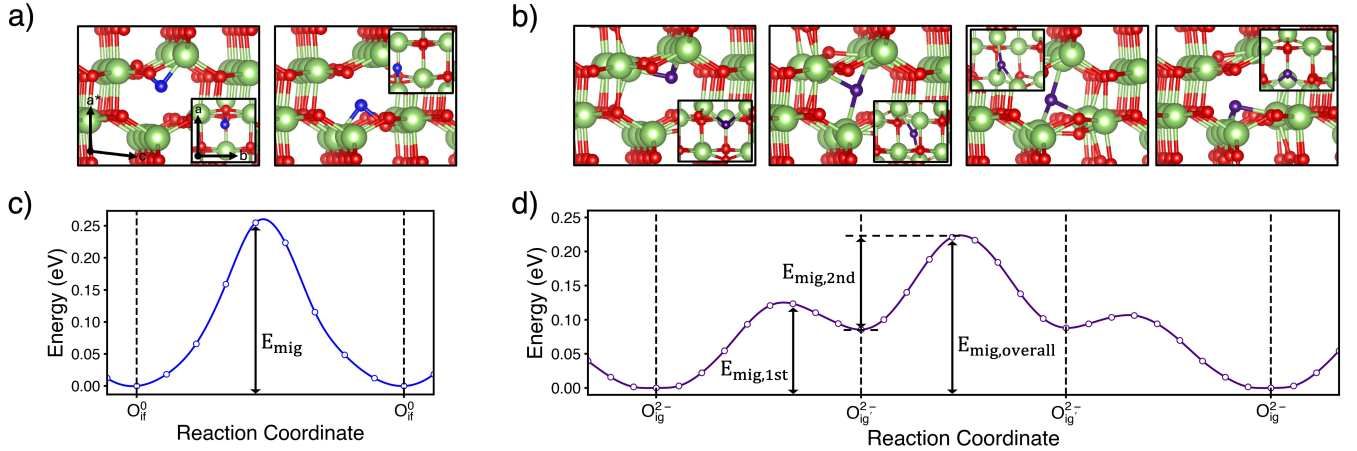


FIG. 5. Dominant b -axis diffusion pathway of (a) O_{if}^0 and (b) O_{ig}^{2-} along with corresponding energy landscapes (c) and (d), respectively, where the energy maxima correspond to 0.25 and 0.24 eV. Dashed lines on the reaction coordinate indicate stable or intermediate configurations.

imperfections in DFT simulations. Both charge states possess sizable anisotropy, with b -axis diffusivity being several orders of magnitude larger than that along the a^* and c -axes. This contrasts with Ga diffusion in β -Ga₂O₃, where diffusion along the c -axis dominates for both interstitials and vacancies [33, 59]. Effective E_{act} for b -axis diffusion are 0.28 eV for the neutral network and 0.24 eV for the charged network, while those of the a^* and c -axes both exceed 1 eV. In the neutral network, $E_{\text{act}}^a = 1.17$ eV and $E_{\text{act}}^c = 1.11$ eV, while $E_{\text{act}}^a = E_{\text{act}}^c = 1.18$ eV in the charged network.

Next, the O_i self-diffusivities (D_{Self,O_i}) are estimated from pre-

dicted D_{O_i} . While D_{O_i} presented above represent the diffusivity of isolated interstitials, they differ from values typically measured in experiment, where the concentration of the diffusing species—and consequently the defect E_{form} —are encompassed. The self-diffusivities are given by

$$D_{\text{Self},O_i} = \frac{[O_i]}{[O_{\text{total}}]} D_{O_i}, \quad (4)$$

where $[O_i]$ is the concentration of migrating O interstitials, $[O_{\text{total}}]$ is the concentration of O sites within the lattice, and D_{O_i} is the diffusivity given in Figure 4(a,e). Detailed chemical potential bound-

aries for O are described in SI Section 4. Figure 4(b-d,f-h) depicts Arrhenius plots for O_i^0 and O_i^{2-} self-diffusivities for a range of thermodynamic conditions. We choose a single E_{Fermi} of 3.0 eV above the VBM (1.8 eV below the conduction band minimum (CBM)) for ease of representation of the neutral (Figure 4(b-d)) and $E_{\text{Fermi}} = 3.8$ eV (0.8 eV below CBM) for the charged plots (Figure 4(f-h)). The different E_{Fermi} correspond to values for which the neutral and ionized interstitial are favorable. Overall, D_{Self,O_i} exhibits similar trends to D_{O_i} : rapid b -axis diffusion dominates, while smaller diffusivities with comparable magnitudes are observed along the a^* - and c -axes. Under O-rich conditions, predicted D_{Self,O_i}^b at 1200 K are 2.34×10^{-18} and 2.37×10^{-13} for the neutral and charged O_i , respectively. Generally, $D_{\text{Self},O_i^{2-}}$ are substantially greater than D_{Self,O_i^0} due to lower E_{form} of the configurations in the charged library, resulting in higher defect concentrations within the crystal.

By systematically removing individual PHs and recalculating diffusivities, we identify the dominant hopping pathways in each crystallographic direction. The dominant diffusion pathways along the fast b -axis for O_i^0 and O_i^{2-} are given in Figure 5(a,b) with corresponding energy profiles along the minimum energy pathway (MEP) in Figure 5(c,d). The dominant neutral pathway (PH 17 in Table S1) depicted in Figure 5(a) features the migration of O_{if}^0 along distinct, well-defined trajectories within the A channel. The migration barrier at the peak of Figure 5(c) is 0.25 eV, enabling remarkably rapid diffusion along the b -axis. Several other PHs between O_{ia}^0 and O_{if}^0 create low-barrier pathways along the b -axis (Figure S2(c,d)), but with slightly larger E_{mig} (Figure S2(e)).

The dominant charged pathway (PH 18 in Table S2), depicted in Figure 5(b), similarly traverses the A channel, but unlike PH 17, it includes an intermediate, metastable state O_{ig}^- (Figure S1(b)). Migration along the MEP in Figure 5(d) begins with the lowest-energy configuration, O_{ig}^{2-} , transitions over the first energy barrier ($E_{\text{mig},1\text{st}} = 0.12$ eV) and proceeds through the intermediate state, O_{ig}^{2-} . It then crosses another energy barrier ($E_{\text{mig},2\text{nd}} = 0.14$ eV) and passes to the next equivalent O_{ig}^{2-} and O_{ig}^{2-} states. This pathway exhibits a slightly smaller overall energy maxima ($E_{\text{mig,overall}} = 0.24$ eV) compared to that of the neutral path, enabling exceptionally fast b -axis diffusion. The formation and breakage of bonds with neighboring Ga atoms likely facilitates the stabilization of O_{ig}^{2-} . Additionally, the 2- charge state could induce higher electrostatic attractions with lattice Ga atoms, further stabilizing the intermediate configurations and slightly lowering the overall barrier. Despite its stability, we exclude O_{ig}^- from our diffusion network because its bonding environment and E_{form} closely resemble those of O_{ig}^- (Figure S1(a,b)). While their states are distinct at 0 K, we expect O_{ig}^- and O_{ig}^- to become nearly identical at slightly elevated T due to additional thermal vibrations. The MEP closely resembles that identified in Zimmermann *et al.*, with intermediate configurations similar to O_{ig}^- (Figure S1(c)) and distinct end states [21]. The migration barrier $E_{\text{mig},2\text{nd}} = 0.14$ for PH 18 matches the E_{mig} reported in Zimmermann *et al.*, potentially suggesting similar local environments or structural constraints shaping the energy landscape.

While significantly smaller, a^* - and c -axis diffusion exhibit interesting behavior. As revealed in Figure 4(a,e), these directions exhibit E_{act} and D_{O_i} that are very similar to each other, not observed in either V_{Ga} or Ga_i diffusion [33]. In the charged network, D_{ca^*} is nearly identical to its pure component counterparts, $D_{a^*a^*}$ and D_{cc} , even at lower temperatures where these differences are among the largest (Figure 6). This suggests that diffusion along the a^* and c -axes is coupled for O_i^{2-} . The ‘‘dominant hop’’ analysis reveals that the same set of principal hops (PH 20, 32, 33, 40 in Table S2) contribute to both a^* and c -axis diffusion. Removing any of these hops reduces

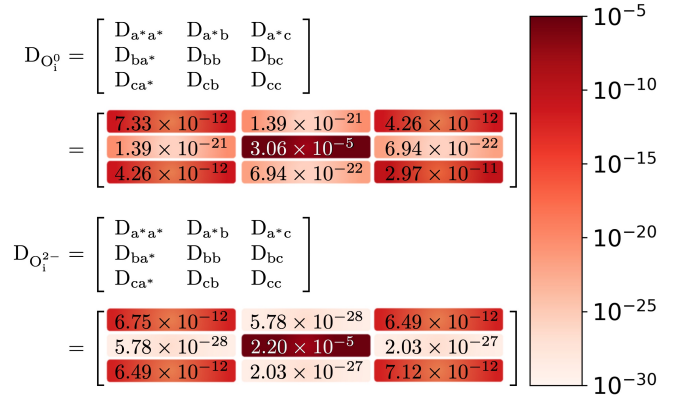


FIG. 6. Three-dimensional diffusivity tensors of O_i^0 and O_i^{2-} at 600 K (cm^2/s).

$D_{a^*a^*}$ and D_{cc} by up to 90%. The PHs 20, 32, and 33 form a fully connected dominant pathway for a^*/c -axis diffusion, as detailed in Figure S2. In the neutral network, D_{ca^*} is smaller than both $D_{a^*a^*}$ and D_{cc} , but remains closer in magnitude to $D_{a^*a^*}$ than to D_{cc} . Removing each dominant a^* -axis hop reduces diffusion exclusively along the a^* -direction, whereas removing dominant c -axis hops substantially decreases diffusion along both a^* and c -directions. This result suggests that diffusion of O_i^0 along the a^* -axis is dependent on some c -axis hops, while c -axis diffusion can exist on its own. The main c -axis pathway and possible a -axis pathways are illustrated in Figures S3 and S4, respectively, where the a -axis pathways highlighted in orange indicate dependence on a c -axis hop.

C. Comparison to Experiments and Oxygen Vacancy Diffusion

Finally, the self-diffusivities in Figure 4(f-h) are compared to previously reported experimental results.

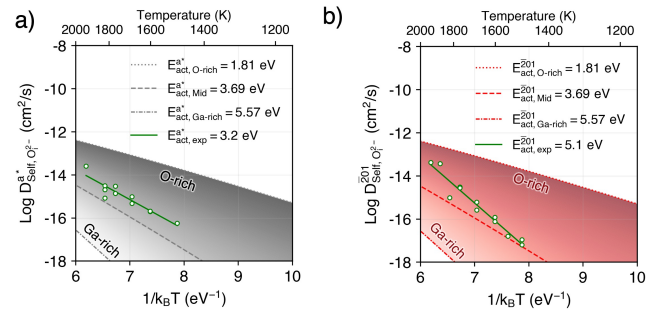


FIG. 7. Arrhenius plots of self-diffusivities with experimental data collected along (a) [100] (Ref. [23]) and (b) [201] (Ref. [24]) from ^{18}O tracer studies. The thermodynamic limits (Ga-rich and O-rich) are given within the dotted lines, where the dashed middle line indicates the midpoint between two limits. Activation energies (E_{act}) for various thermodynamic conditions are indicated.

Figure 7 presents experimentally measured D_{Self,O_i} and E_{act} from Uhlendorf *et al.*, obtained from ^{18}O tracer experiments conducted at temperatures between 1400 and 2000 K in unintentionally doped

(UID) β -Ga₂O₃ along (a) [100] [23] and (b) $\bar{2}01$ [24]. The measured $D_{\text{Self},\text{O}_i}$ fall within the range of our prediction for O_i^{2-} within the slightly O-rich region, consistent with our expectation given the experimental setup [23–25]. Our predicted E_{act} ranges from 1.81 (O-rich) to 5.57 eV (Ga-rich) along [100] and $\bar{2}01$, when E_{Fermi} is 3.8 eV. The experimentally measured E_{act}^{100} of 3.2 ± 0.4 and E_{act}^{201} of 5.0 ± 0.4 eV lie in the predicted range of our predictions [23, 24]. It is worth noting that these predicted ranges are sensitive to the position of E_{Fermi} , which can make direct comparisons with experimental data difficult. Nevertheless, the overall consistency between our findings and experimental measurements on $D_{\text{Self},\text{O}_i}$ and E_{act} highlights the robustness and reliability of our approach.

We also compare our E_{act} for O_i self-diffusion with estimated E_{act} values for V_O self-diffusion, derived from previously reported E_{for} and E_{mig} from first-principles calculations, to assess whether O self-diffusion in β -Ga₂O₃ is most dominantly interstitial- or vacancy-mediated. We adopt the range of E_{for} values from Kyrtsov et al. (3.8–4.6 eV) under O-rich and n-doped conditions, along with E_{mig} (1.2–2.7 eV) [49]. By adding these E_{for} and E_{mig} , we estimate E_{act} of V_O self-diffusion between 5.0–7.3 eV, which is far beyond our predicted range for O_i self-diffusion $E_{\text{act}, \text{O-rich}}$ between 0.86–2.85 eV (Figure 4). Overall, our results are in agreement with Uhlendorf *et al.*'s hypothesis suggesting that O diffusion in β -Ga₂O₃ is likely governed by O_i , not V_O [23–25].

IV. CONCLUSION

From first-principles calculations, we investigated various oxygen defects in β -Ga₂O₃, including split-interstitial configurations, and examined the associated diffusion pathways. Employing the Onsager formalism, we developed and solved the master diffusion equations for O_i^0 and O_i^{2-} under detailed balance, yielding three-dimensional diffusivity tensors. Our results revealed that the b -axis enables the fastest diffusion, with diffusivities of 2.30×10^{-4} cm²/s and 6.33×10^{-5} cm²/s at 1200 K, and corresponding effective activation energies of 0.28 and 0.24 eV for O_i^0 and O_i^{2-} , respectively.

At O-rich conditions, we predicted self-diffusivities of 2.34×10^{-18} and 2.37×10^{-13} cm²/s along the b -axis at 1200 K, for O_i^0 and O_i^{2-} , respectively. We identified the most dominant diffusion pathways along each crystallographic direction and found that O self-diffusion is likely mediated by interstitials, consistent with reported ¹⁸O tracer diffusion experiments. Our findings expand our insights into mass transport and defect-mediated degradation mechanisms in β -Ga₂O₃, contributing to a broader perspective on defect diffusion in semiconducting oxides.

V. SUPPLEMENTARY MATERIAL

See supporting information for Tables S1 and S2, Figures S1-S5, and details on oxygen chemical potential boundary selection.

VI. ACKNOWLEDGMENT

GM and EE acknowledge support from the U.S. National Science Foundation (NSF) via Grant No. 1922758 (DIGI-MAT). CL and EE acknowledge funding provided by the Air Force Office of Scientific Research under Award No. FA9550-21-0078 (Program Manager: Dr. Ali Sayir). This work used PSC Bridges-2 at the Pittsburgh Supercomputing Center through allocation MAT220011 from the Advanced Cyberinfrastructure Coordination Ecosystem: Services & Support (ACCESS) program, which is supported by National Science Foundation grants #2138259, #2138286, #2138307, #2137603, and #2138296.

VII. DATA AVAILABILITY

The data that supports the findings of this study are available on GitHub at <https://github.com/ertekin-research-group/2025-Ga2O3-O-Diffusion>.

-
- [1] H. H. Tippins, Phys. Rev. **140**, A316 (1965).
 - [2] T. Matsumoto, M. Aoki, A. Kinoshita, and T. Aono, Japanese Journal of Applied Physics **13**, 1578 (1974).
 - [3] N. Ueda, H. Hosono, R. Waseda, and H. Kawazoe, Applied Physics Letters **71**, 933 (1997).
 - [4] M. Higashiwaki, K. Sasaki, A. Kuramata, T. Masui, and S. Yamakoshi, Applied Physics Letters **100**, 013504 (2012).
 - [5] E. G. Villora, K. Shimamura, T. Ujiie, and K. Aoki, Applied Physics Letters **92**, 202118 (2008).
 - [6] Z. Galazka, K. Irmscher, R. Uecker, R. Bertram, M. Pietsch, A. Kwasniewski, M. Naumann, T. Schulz, R. Schewski, D. Klimm, and M. Bickermann, Journal of Crystal Growth **404**, 184 (2014).
 - [7] A. J. Green, J. Speck, G. Xing, P. Moens, F. Allerstam, K. Gumaelius, T. Neyer, A. Arias-Purdue, V. Mehrotra, A. Kuramata, K. Sasaki, S. Watanabe, K. Koshi, J. Blevins, O. Bierwagen, S. Krishnamoorthy, K. Leedy, A. R. Arehart, A. T. Neal, S. Mou, S. A. Ringel, A. Kumar, A. Sharma, K. Ghosh, U. Singiseti, W. Li, K. Chabak, K. Liddy, A. Islam, S. Rajan, S. Graham, S. Choi, Z. Cheng, and M. Higashiwaki, APL Materials **10**, 029201 (2022).
 - [8] S. J. Pearton, J. Yang, I. Cary, Patrick H., F. Ren, J. Kim, M. J. Tadjer, and M. A. Mastro, Applied Physics Reviews **5**, 011301 (2018).
 - [9] H. Huang, L. Wang, H. Zhou, H. Xing, L. Wang, W. Zhang, K. Tang, J. Huang, and L. Wang, ACS Applied Materials & Interfaces 10.1021/acsami.4c15345 (2024).
 - [10] A. Pérez-Tomás, E. Chikoidze, Y. Dumont, M. Jennings, S. Russell, P. Vales-Castro, G. Catalan, M. Lira-Cantú, C. Ton-That, F. Teherani, V. Sandana, P. Bove, and D. Rogers, Materials Today Energy **14**, 100350 (2019).
 - [11] S. Giri, B. Mahata, P. K. Guha, and P. Banerji, ACS Applied Electronic Materials **6**, 230 (2024).
 - [12] H. Aida, K. Nishiguchi, H. Takeda, N. Aota, K. Sunakawa, and Y. Yaguchi, Japanese Journal of Applied Physics **47**, 8506 (2008).
 - [13] G. Feng, S. Li, Y. Tian, S. Qi, D. Guo, and W. Tang, ACS Omega **9**, 22084 (2024).
 - [14] T. Takeuchi, H. Ishikawa, N. Takeuchi, and Y. Horikoshi, Thin Solid Films **516**, 4593 (2008), 6th International Conference on Coatings on Glass and Plastics (ICCG6)- Advanced Coatings for Large-Area or High-Volume Products-.

- [15] M. Higashiwaki, K. Sasaki, A. Kuramata, T. Masui, and S. Yamakoshi, *physica status solidi (a)* **211**, 21 (2014).
- [16] M. Orita, H. Ohta, M. Hirano, and H. Hosono, *Applied Physics Letters* **77**, 4166 (2000).
- [17] S. G. Motti, J. B. Patel, R. D. J. Oliver, H. J. Snaith, M. B. Johnston, and L. M. Herz, *Nature Communications* **12**, 6955 (2021).
- [18] M. M. Kabir and D. E. Demirocak, *International Journal of Energy Research* **41**, 1963 (2017).
- [19] J. Jeong, N. Aetukuri, T. Graf, T. D. Schladt, M. G. Samant, and S. S. P. Parkin, *Science* **339**, 1402 (2013).
- [20] J. Meng, M. S. Sheikh, R. Jacobs, J. Liu, W. O. Nachlas, X. Li, and D. Morgan, *Nature Materials* **23**, 1252 (2024).
- [21] C. Zimmermann, V. Rønning, Y. Kalmann Frodason, V. Bobal, L. Vines, and J. B. Varley, *Phys. Rev. Mater.* **4**, 074605 (2020).
- [22] H. Jeong, E. Ertekin, and E. G. Seebauer, *ACS Applied Materials & Interfaces* **14**, 34059 (2022).
- [23] J. Uhlendorf, Z. Galazka, and H. Schmidt, *Applied Physics Letters* **119**, 242106 (2021).
- [24] J. Uhlendorf and H. Schmidt, *Phys. Rev. Mater.* **7**, 093402 (2023).
- [25] J. Uhlendorf and H. Schmidt, *Zeitschrift für Naturforschung B* **79**, 225 (2024).
- [26] A. F. Kohan, G. Ceder, D. Morgan, and C. G. Van de Walle, *Phys. Rev. B* **61**, 15019 (2000).
- [27] H. Peelaers, J. L. Lyons, J. B. Varley, and C. G. Van de Walle, *APL Materials* **7**, 10.1063/1.5063807 (2019), 022519.
- [28] C. Lee, N. D. Rock, A. Islam, M. A. Scarpulla, and E. Ertekin, *APL Materials* **11**, 10.1063/5.0131453 (2023), 011106.
- [29] K. Alberi and M. Scarpulla, *Scientific Reports* **6**, 10.1038/srep27954 (2016).
- [30] S. B. Zhang, S.-H. Wei, and A. Zunger, *Phys. Rev. B* **63**, 075205 (2001).
- [31] P. G. Moses, A. Janotti, C. Franchini, G. Kresse, and C. G. Van de Walle, *Journal of Applied Physics* **119**, 181503 (2016).
- [32] H. Jeong and E. G. Seebauer, *Journal of Vacuum Science & Technology A* **41**, 033203 (2023).
- [33] C. Lee, M. A. Scarpulla, and E. Ertekin, *Phys. Rev. Mater.* **8**, 054603 (2024).
- [34] D. R. Trinkle, *Philosophical Magazine* **96**, 2714 (2016).
- [35] D. R. Trinkle, *Philosophical Magazine* **97**, 2514 (2017).
- [36] D. Trinkle and A. Jain, *Dallastrinkle/onsager: Onsager v1.3.3* (2019).
- [37] S. J. Honrao, Q. Rizzardi, R. Maaß, D. R. Trinkle, and R. G. Hennig, *Phys. Rev. Mater.* **4**, 103608 (2020).
- [38] A. Goyal, P. Gorai, H. Peng, S. Lany, and V. Stevanović, *Computational Materials Science* **130**, 1 (2017).
- [39] M. E. Ingebrigtsen, A. Y. Kuznetsov, B. G. Svensson, G. Alfieri, A. Mihaila, U. Badstübner, A. Perron, L. Vines, and J. B. Varley, *APL Materials* **7**, 10.1063/1.5054826 (2018), 022510.
- [40] M. Uddin Jewel, S. Hasan, and I. Ahmad, *Computational Materials Science* **218**, 111950 (2023).
- [41] Y. Huang, X. Xu, J. Yang, X. Yu, Y. Wei, T. Ying, Z. Liu, Y. Jing, W. Li, and X. Li, *Materials Today Communications* **35**, 105898 (2023).
- [42] P. Hohenberg and W. Kohn, *Physical Review* **136**, B864 (1964).
- [43] W. Kohn and L. J. Sham, *Physical Review* **140**, A1133 (1965).
- [44] P. E. Blöchl, *Phys. Rev. B* **50**, 17953 (1994).
- [45] G. Kresse and D. Joubert, *Phys. Rev. B* **59**, 1758 (1999).
- [46] G. Kresse and J. Furthmüller, *Physical Review B* **54**, 11169 (1996).
- [47] G. Kresse and J. Furthmüller, *Computational Materials Science* **6**, 15 (1996).
- [48] J. P. Perdew, K. Burke, and M. Ernzerhof, *Phys. Rev. Lett.* **77**, 3865 (1996).
- [49] A. Kyrtsos, M. Matsubara, and E. Bellotti, *Phys. Rev. B* **95**, 245202 (2017).
- [50] S. Yoshioka, H. Hayashi, A. Kuwabara, F. Oba, K. Matsunaga, and I. Tanaka, *Journal of Physics: Condensed Matter* **19**, 346211 (2007).
- [51] T. Zacherle, P. C. Schmidt, and M. Martin, *Phys. Rev. B* **87**, 235206 (2013).
- [52] S. Geller, *The Journal of Chemical Physics* **33**, 676 (1960).
- [53] J. Åhman, G. Svensson, and J. Albertsson, *Acta Crystallographica Section C* **52**, 1336 (1996).
- [54] H. J. Monkhorst and J. D. Pack, *Phys. Rev. B* **13**, 5188 (1976).
- [55] C. Freysoldt, B. Grabowski, T. Hickel, J. Neugebauer, G. Kresse, A. Janotti, and C. G. Van de Walle, *Rev. Mod. Phys.* **86**, 253 (2014).
- [56] S. Lany and A. Zunger, *Modelling and Simulation in Materials Science and Engineering* **17**, 084002 (2009).
- [57] J. M. Adamczyk, L. C. Gomes, J. Qu, G. A. Rome, S. M. Baumann, E. Ertekin, and E. S. Toberer, *Chemistry of Materials* **33**, 359 (2021).
- [58] G. Henkelman, B. P. Uberuaga, and H. Jónsson, *Journal of Chemical Physics* **113**, 9901 (2000).
- [59] Y. K. Frodason, P. P. Krzyzaniak, L. Vines, J. B. Varley, C. G. Van de Walle, and K. M. H. Johansen, *APL Materials* **11**, 10.1063/5.0142671 (2023), 041121.
- [60] M. A. Blanco, M. B. Sahariah, H. Jiang, A. Costales, and R. Pandey, *Phys. Rev. B* **72**, 184103 (2005).
- [61] J. Lehtomäki, J. Li, and P. Rinke, *Journal of Physics Communications* **4**, 125001 (2020).
- [62] B. R. Tuttle, N. J. Karom, A. O'Hara, R. D. Schrimpf, and S. T. Pantelides, *Journal of Applied Physics* **133**, 015703 (2023).
- [63] P. Deák, Q. Duy Ho, F. Seemann, B. Aradi, M. Lorke, and T. Frauenheim, *Phys. Rev. B* **95**, 075208 (2017).
- [64] D. Sun, Y. Gao, J. Xue, and J. Zhao, *Journal of Alloys and Compounds* **794**, 374 (2019).
- [65] Q. Li, J. Zhao, Y. Li, X. Guan, Z. Jia, N. Lin, and X. Zhao, *The Journal of Physical Chemistry C* **128**, 11817 (2024).
- [66] N. R. Martins, L. A. F. de Campos Viana, A. A. das Graças Santos, D. D. Borges, E. Welch, P. D. Borges, and L. Scolfaro, *Journal of Vacuum Science & Technology A* **42**, 032801 (2024).

Supporting Information for Investigation of O interstitial diffusion in β -Ga₂O₃: a direct approach via master diffusion equations

Grace McKnight,[†] Channyung Lee,[†] and Elif Ertekin^{*,†,‡}

[†]*Department of Mechanical Science and Engineering, University of Illinois at
Urbana-Champaign, 1206 W. Green Street, Urbana, Illinois 61801, United States.*

[‡]*Materials Research Laboratory, University of Illinois at Urbana-Champaign, Urbana,
Illinois 61801*

E-mail: ertekin@illinois.edu

Table S1: A list of principle hops (PHs), which cannot be further decomposed into multiple shorter elementary hops, between O_i^0 configurations and their corresponding migration barriers in forward (\rightarrow) and backward (\leftarrow) directions. The migration barriers were calculated by the ci-NEB method using the PBE functional as described in Section II.

Principle hop (PH)	Transformation	Distance (\AA)	\rightarrow (eV)	\leftarrow (eV)
1	$O_{ia}^0 \rightleftharpoons O_{ia}^0$	2.95	0.85	0.85
2	$O_{ia}^0 \rightleftharpoons O_{ia}^0$	0.14	0.08	0.08
3	$O_{ia}^0 \rightleftharpoons O_{ib}^0$	2.89	1.10	0.35
4	$O_{ia}^0 \rightleftharpoons O_{id}^0$	2.80	0.88	0.65
5	$O_{ia}^0 \rightleftharpoons O_{if}^0$	0.42	0.27	0.22
6	$O_{ia}^0 \rightleftharpoons O_{if}^0$	2.92	0.3	0.25
7	$O_{ib}^0 \rightleftharpoons O_{ib}^0$	2.62	0.50	0.50
8	$O_{ib}^0 \rightleftharpoons O_{ic}^0$	0.26	0.39	0.85
9	$O_{ib}^0 \rightleftharpoons O_{ie}^0$	2.63	1.17	1.71
10	$O_{ic}^0 \rightleftharpoons O_{ic}^0$	2.58	0.59	0.59
11	$O_{ic}^0 \rightleftharpoons O_{ie}^0$	2.57	0.39	0.88
12	$O_{id}^0 \rightleftharpoons O_{ie}^0$	0.35	0.31	0.40
13	$O_{id}^0 \rightleftharpoons O_{ie}^0$	3.11	1.22	1.31
14	$O_{id}^0 \rightleftharpoons O_{if}^0$	2.80	1.41	1.59
15	$O_{ie}^0 \rightleftharpoons O_{ie}^0$	3.31	1.34	1.34
16	$O_{ie}^0 \rightleftharpoons O_{ie}^0$	3.08	0.88	0.88
17	$O_{if}^0 \rightleftharpoons O_{if}^0$	2.71	0.25	0.25

Table S2: A list of principle hops (PHs), which cannot be further decomposed into multiple shorter elementary hops, between O_i^{2-} configurations and their corresponding migration barriers in forward (\rightarrow) and backward (\leftarrow) directions. The migration barriers were calculated by the ci-NEB method using the PBE functional as described in Section II.

Principle hop (PH)	Transformation	Distance (\AA)	\rightarrow (eV)	\leftarrow (eV)
18	$O_{ig}^{2-} \rightleftharpoons O_{ig}^{2-}$	2.14	0.24	0.24
19	$O_{ig}^{2-} \rightleftharpoons O_{ig}^{2-}$	3.09	2.18	2.18
20	$O_{ig}^{2-} \rightleftharpoons O_{ih}^{2-}$	1.45	1.12	0.61
21	$O_{ig}^{2-} \rightleftharpoons O_{ih}^{2-}$	1.64	0.71	0.19
22	$O_{ig}^{2-} \rightleftharpoons O_{ih}^{2-}$	3.32	0.71	0.20
23	$O_{ig}^{2-} \rightleftharpoons O_{ih}^{2-}$	3.50	2.76	2.24
24	$O_{ig}^{2-} \rightleftharpoons O_{ii}^{2-}$	3.88	2.72	1.50
25	$O_{ig}^{2-} \rightleftharpoons O_{ij}^{2-}$	3.49	3.36	2.29
26	$O_{ig}^{2-} \rightleftharpoons O_{ik}^{2-}$	3.92	1.44	0.76
27	$O_{ih}^{2-} \rightleftharpoons O_{ih}^{2-}$	3.09	0.33	0.33
28	$O_{ih}^{2-} \rightleftharpoons O_{ih}^{2-}$	3.53	2.99	2.99
29	$O_{ih}^{2-} \rightleftharpoons O_{ih}^{2-}$	3.72	2.96	2.96
30	$O_{ih}^{2-} \rightleftharpoons O_{ii}^{2-}$	1.88	0.80	0.10
31	$O_{ih}^{2-} \rightleftharpoons O_{ij}^{2-}$	3.80	2.63	2.09
32	$O_{ih}^{2-} \rightleftharpoons O_{ik}^{2-}$	1.59	0.47	0.30
33	$O_{ih}^{2-} \rightleftharpoons O_{ik}^{2-}$	2.27	0.71	0.54
34	$O_{ii}^{2-} \rightleftharpoons O_{ii}^{2-}$	1.31	0.72	0.72
35	$O_{ii}^{2-} \rightleftharpoons O_{ii}^{2-}$	1.78	0.74	0.74
36	$O_{ii}^{2-} \rightleftharpoons O_{ik}^{2-}$	0.66	0.00	0.54
37	$O_{ii}^{2-} \rightleftharpoons O_{ik}^{2-}$	1.37	0.36	0.90
38	$O_{ij}^{2-} \rightleftharpoons O_{ij}^{2-}$	1.52	0.79	0.79
39	$O_{ij}^{2-} \rightleftharpoons O_{ij}^{2-}$	1.57	0.66	0.66
40	$O_{ij}^{2-} \rightleftharpoons O_{ik}^{2-}$	2.85	0.15	0.53
41	$O_{ik}^{2-} \rightleftharpoons O_{ik}^{2-}$	1.10	0.30	0.30
42	$O_{ik}^{2-} \rightleftharpoons O_{ik}^{2-}$	1.30	0.59	0.59
43	$O_{ik}^{2-} \rightleftharpoons O_{ik}^{2-}$	1.70	1.28	1.28
44	$O_{ik}^{2-} \rightleftharpoons O_{ik}^{2-}$	1.99	0.84	0.84
45	$O_{ik}^{2-} \rightleftharpoons O_{ik}^{2-}$	3.09	0.86	0.86

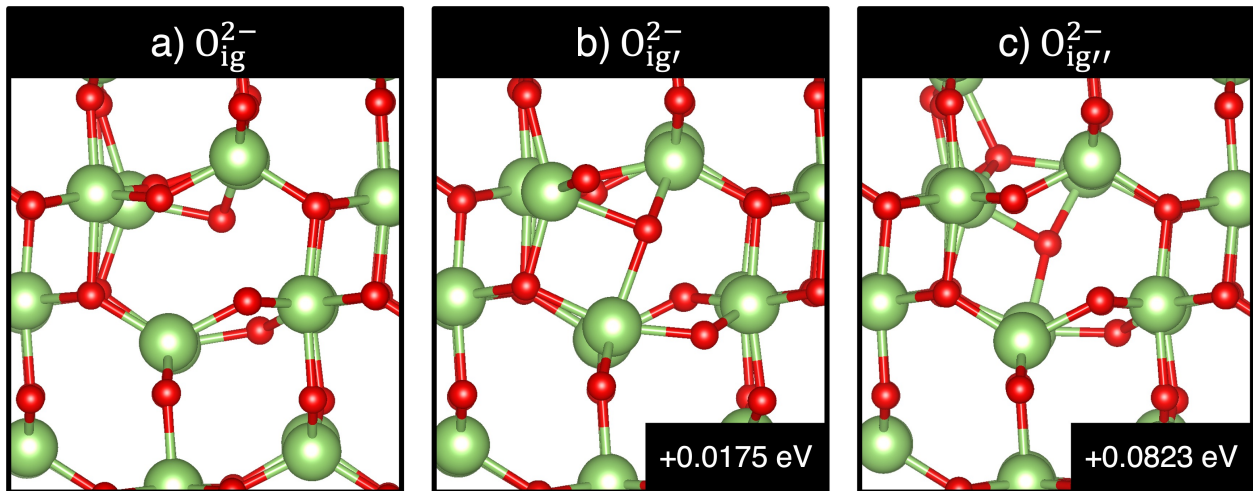


Figure S1: Configurations of (a) O_{ig}^{2-} , (b) $O_{ig'}^{2-}$, and (c) $O_{ig''}^{2-}$ within the A channel. Energies given in the bottom right corners of (b) and (c) are relative to $E_{\text{for}}[O_{ig}^{2-}]$.

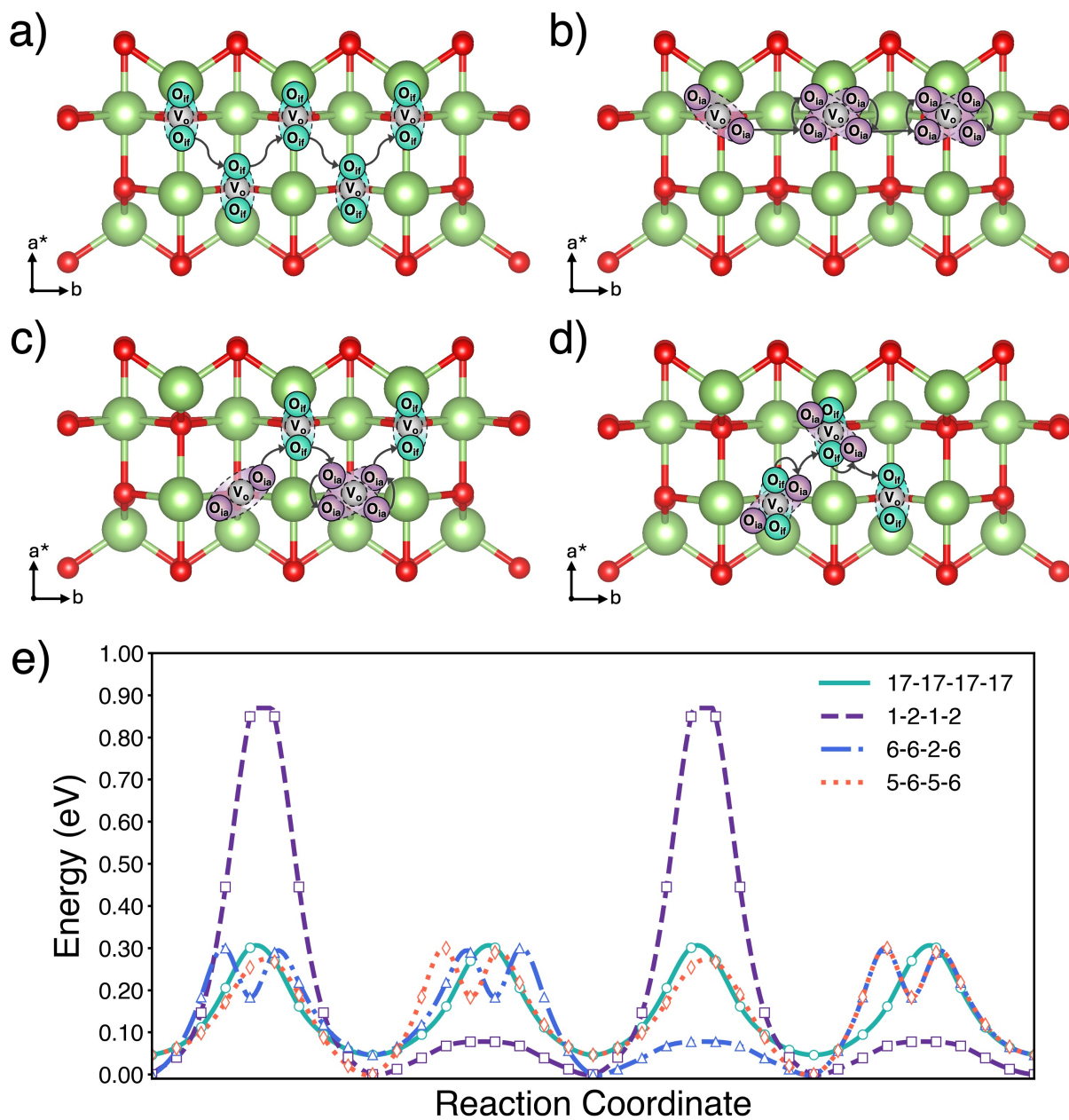


Figure S2: (a-d) Schematic representation of some possible (010) diffusion pathways of neutral ($q = 0$) oxygen interstitials and (e) corresponding energies along the energy minimum pathways. The pathways consist of principle hops (PHs) (a) 17-17-17-17, (b) 1-2-1-2 (c) 6-6-2-6, and (d) 5-6-5-6.

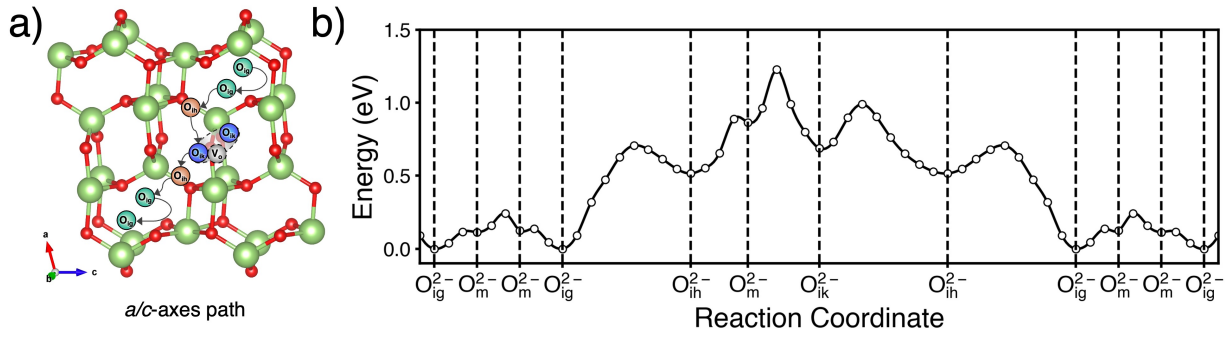


Figure S3: (a) Schematic representation of the dominant [100] and [001] diffusion pathway of charged ($q = 2-$) oxygen interstitials and (b) corresponding energies along the energy minimum pathway. Dashed lines in (b) indicate a configuration in the network or intermediate configuration (O_{ig}^{2-} , O_{ik}^{2-}).

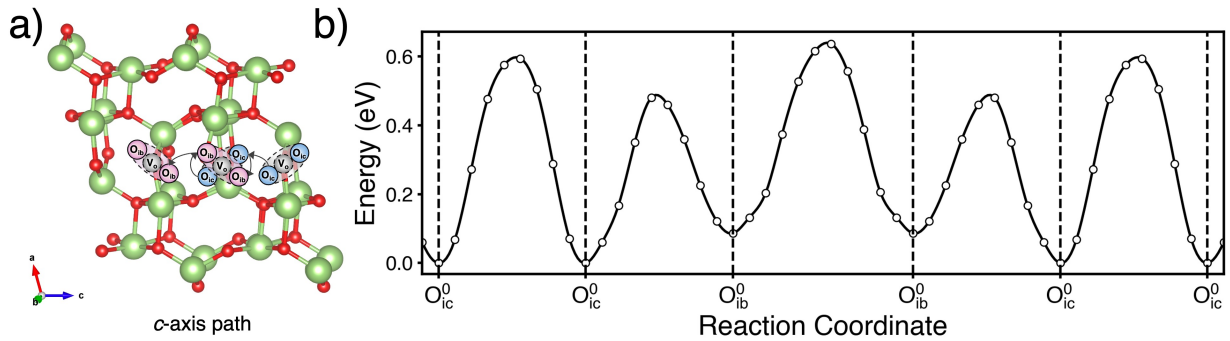


Figure S4: (a) Schematic representation of the dominant [001] diffusion pathway of neutral ($q = 0$) oxygen interstitials and (b) corresponding energies along the energy minimum pathway. Dashed lines in (b) indicate configurations in the network.

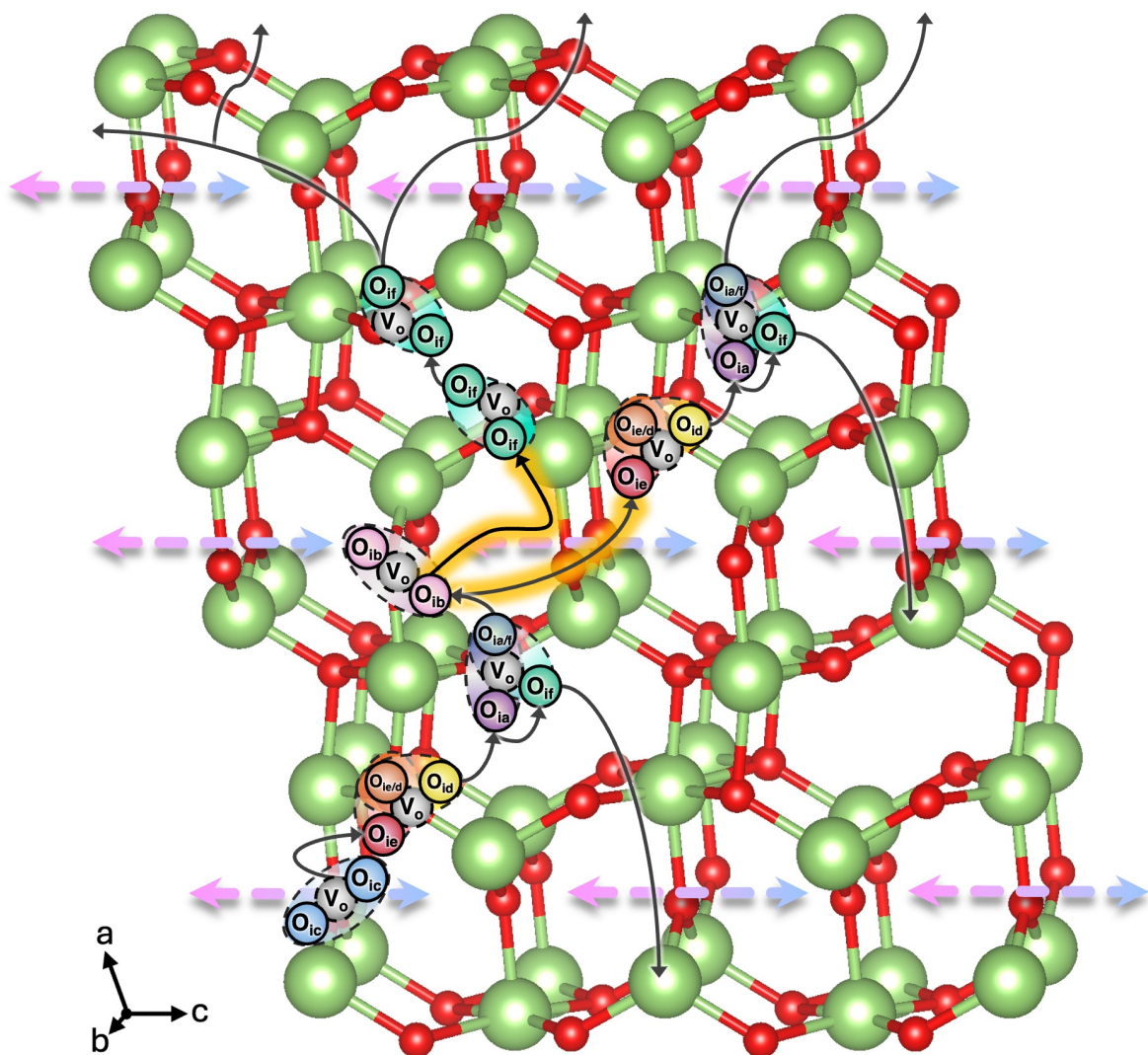


Figure S5: Schematic representation of the dominant [100] diffusion pathway of neutral ($q = 0$) oxygen interstitials. Black arrows show potential pathways of the neutral interstitial. The dashed double arrows represent the availability of a [001] hop along the diffusion pathway in Figure S4. Highlighted black arrows emphasize necessary [001] hops along the [001] pathways.

Oxygen Chemical Potential Boundaries

To establish appropriate chemical potential boundaries for the oxygen chemical potential μ_{O} , we use

$$\mu_{\text{O}} = \mu_{\text{O}}^0(T) + \Delta\mu_{\text{O}}(T), \quad (1)$$

where $\Delta\mu_{\text{O}}(T)$ represents the deviation from oxygen rich conditions ($\Delta\mu_{\text{O}}(T) = 0$). At the other extreme, oxygen poor conditions, $\Delta\mu_{\text{O}}(T) = (1/3)\Delta H_f(\beta\text{-Ga}_2\text{O}_3)$ where $\Delta H_f(\beta\text{-Ga}_2\text{O}_3) = -10.78$ eV/fu is the computed E_f of $\beta\text{-Ga}_2\text{O}_3$ (the negative value indicates favorable Ga_2O_3 formation). The reference state $\mu_{\text{O}}^0(T)$ is defined as half of the energy of an O_2 molecule. This reference is obtained from DFT calculations ($T = 0$ K), and with a correction term to account for the PBE overbinding of the molecule [1]. The region enclosed in dotted lines varies from Ga-rich (low $p(\text{O}_2)$) to O-rich (high $p(\text{O}_2)$), with the dashed midpoint for reference. These chemical potential boundaries ensure that the calculated defect E_f are consistent with the thermodynamic limits of the system.

References

- [1] D. Patton, D. Porezag, and M. Pederson, *Phys. Rev. B*, **55**, 7454 (1997).